JOURNAL OF SYNCHROTRON RADIATION
ISSN 1600-5775

Identification of spatial magnetic inhomogeneities by nuclear forward scattering of synchrotron radiation

Vlastimil Vrba,[a]* Vít Procházka[a] and Marcel Miglierini[b,c]

[a]Department of Experimental Physics, Faculty of Science, Palacký University Olomouc, 17 listopadu 1192/12, 771 46 Olomouc, Czech Republic, [b]Institute of Nuclear and Physical Engineering, Faculty of Electrical Engineering and Information Technology, Slovak University of Technology in Bratislava, Ilkovičova 3, 812 19 Bratislava, Slovakia, and [c]Department of Nuclear Reactors, Faculty of Nuclear Sciences and Physical Engineering, Czech Technical University in Prague, V Holešovičkách 2, 180 00 Prague, Czech Republic. *Correspondence e-mail: vlastimil.vrba@upol.cz

Received 29 November 2018
Accepted 18 April 2019

Edited by G. Grübel, HASYLAB at DESY, Germany

Keywords: nuclear forward scattering; magnetic inhomogeneities; rotational invariance; Mössbauer spectroscopy; metallic glasses.

Spatially confined magnetic inhomogeneities were revealed by measuring nuclear forward scattering time spectra on the same sample in two different geometric arrangements. They differ by 180° rotation of the sample around one of the polarization axes. A basic theoretical description of this phenomenon and its relation to a spatial distribution of nuclei featuring different magnetic moments is provided. From an experimental point of view, the violation of rotational invariance was observed for an inhomogeneous $Fe_{81}Mo_8Cu_1B_{10}$ metallic glass. The development of magnetic inhomogeneities and their relation to the evolution of time spectra was studied during thermal annealing.

1. Introduction

High-brilliance synchrotron radiation has opened new possibilities for the utilization of nuclear resonant scattering (Rüffer, 2002). Nuclear forward scattering (NFS), which can be used for the investigation of hyperfine interactions within solid-state samples, is currently one of the most rapidly developing synchrotron methods. It has successfully been applied to investigating diffusion, magnetic ordering or structural/phase transformation kinetics (Vogl & Sepiol, 1999; Miglierini *et al.*, 2012, 2015; Machala *et al.*, 2015).

This study reports on the noncommutative nature of NFS and its use for investigating inhomogeneous samples. This can be observed experimentally as a difference in the time spectra measured before and after a sample rotation around one of the polarization axes by 180°. Similar behaviour has also been studied in connection with the reciprocity phenomenon and its violation in scattering experiments (Deák *et al.*, 2012). Here the observed violation of the 180° rotational invariance, which in general differs from the reciprocity violation, is caused by the internal properties of the measured sample. This brings new possibilities for investigating hyperfine interactions in inhomogeneous systems. Consequently, a simple two-step identification of nuclei featuring an inhomogeneous spatial distribution of their corresponding hyperfine interactions along the direction of the incoming radiation is possible. There are only a limited number of experimental techniques which allow the observation of bulk inhomogeneities of hyperfine interactions (Cashion *et al.*, 1990; Smith *et al.*, 1992; Atzmony *et al.*, 1987).

This article is composed of two parts. In the first part, we describe the rotational invariance violation and discuss the conditions for its observation. The second part demonstrates

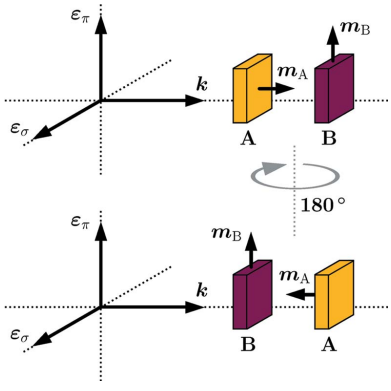

the feasibility of this approach applied to iron-based amorphous and nanocrystalline alloys, where information on the inhomogeneity and its evolution with time during isothermal annealing could be achieved solely from two independent NFS experiments.

2. Rotational invariance violation by inhomogeneous distribution of hyperfine fields

2.1. Theoretical treatment

Scattering from a macroscopic system of thickness d and resonant nuclei density ρ can be described by an energy-dependent 2×2 scattering matrix (Röhlsberger, 2004; L'Abbé *et al.*, 2001),

$$T = \exp\left(\frac{i\,2\pi\rho N d}{k}\right), \tag{1}$$

with k being the radiation wavenumber and N the scattering length, which depends on the multipolarity of the Mössbauer transition.

For ^{57}Fe with a magnetic dipole ($M1$) transition (Sturhahn & Gerdau, 1994), the scattering length matrix elements are given by the formula

$$N_{\mu\nu} = \frac{4\pi}{k} \sum_{M'=-1}^{1} \sum_{M=-1}^{1} \left[\boldsymbol{\varepsilon}_{\nu}^{*} \cdot \mathbf{Y}_{M'}\right]\left[\mathbf{Y}_{M}^{*} \cdot \boldsymbol{\varepsilon}_{\mu}\right] F_{M'M}, \tag{2}$$

where $\mathbf{Y}_M$ are vector spherical harmonics corresponding to the $M1$ transition and which depend on the radiation wavevector $\mathbf{k}$ direction, and μ and ν are index parameters of the matrix elements in the chosen polarization $\boldsymbol{\varepsilon}_{\mu,\nu}$ basis. The energy-dependent functions $F_{M'M}$ contain information on the hyperfine interactions described by a set of parameters including the hyperfine magnetic field and the electric-field gradient tensor and their orientations.

The resulting spectra that correspond to the scattered radiation intensity can be fully described by the scattering matrix elements. The scattered radiation can be evaluated in the energy or time domain. The transition from the energy to the time domain, which corresponds to NFS, is achieved via a Fourier transform. The problem is often treated using a linear polarization basis ($\boldsymbol{\varepsilon}_{\sigma}$, $\boldsymbol{\varepsilon}_{\pi}$), where $\boldsymbol{\varepsilon}_{\sigma}$ lies in the plane of the accelerator storage ring and $\boldsymbol{\varepsilon}_{\pi}$ is perpendicular to this plane.

The scattering length (2) corresponds to a given nuclear site (local environment of nuclei). In the case of multiple nuclear sites, *e.g.* non-equivalent crystal sublattices, homogeneously distributed in the system, N can be taken as the sum of the scattering lengths N_i of the individual sites

$$N = \sum_{i=1}^{n} w_i N_i, \tag{3}$$

where each scattering length depends on an individual set of hyperfine parameters including the corresponding relative weights w_i ($\sum_{i=1}^{n} w_i = 1$). From the rotational properties of polarization and spherical harmonics vectors, one can find that 180° rotation of such a homogeneous system around one of the polarization axes, defined by the vectors $\boldsymbol{\varepsilon}_{\sigma}$ and $\boldsymbol{\varepsilon}_{\pi}$, does not affect the intensity of the transmitted radiation.

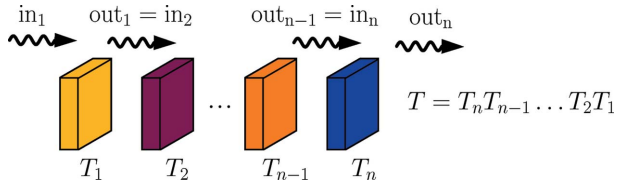

Figure 1
A schematic illustration of a scattering system which consists of n layers described by partial scattering matrices T_i. The wave transmitted through the jth layer described by T_j is the incoming wave for the following layer described by T_{j+1} (*i.e.* out$_j$ = in$_{j+1}$) and in general differs from in$_j$.

Rotational invariance violation for nuclear sites inhomogeneously distributed along the $\mathbf{k}$ direction can be demonstrated on a multilayered system where each layer contains different homogeneously distributed sites described by N_i and T_i. The radiation transmitted through the previous layer can then be treated as incident radiation for the next layer. Therefore, the total scattering matrix T is given by a multiplication of matrices T_i (Fig. 1).

For the simple case of two layers, T reduces to

$$T = T_2 T_1 = \exp\left(\frac{i\,2\pi\rho_2 N_2 d_2}{k}\right) \exp\left(\frac{i\,2\pi\rho_1 N_1 d_1}{k}\right). \tag{4}$$

When N_1 and N_2 commute, their exponentials commute too, and so $T_2T_1 = T_1T_2$. In such a case the scattering is not influenced by the order of the layers, *i.e.* whether the incident radiation hits layer 1 first and then layer 2 or *vice versa*. Moreover, the commutativity also ensures that when the system is rotated by 180° around one of the polarization axes, the corresponding scattering matrix $T^{\rm rot} = (T_2T_1)^{\rm rot}$ differs from T only in the signs of its off-diagonal matrix elements. Assuming linearly polarized (or unpolarized) incident radiation, this does not affect the resulting intensity. Consequently, the system behaves as homogeneous and the scattered radiation intensity is the same for both sample orientations. However, in the general case the commutativity is not satisfied and therefore a difference in the scattered intensities may be observed. In other words, noncommutativity of the scattering lengths N_i is a necessary condition for rotational invariance violation.

The noncommutativity condition brings an important physical requirement for the scattering system. Differences in the time spectra can be observed only when the system exhibits a preferential orientation of electric and/or magnetic fields, *i.e.* texture (Pfannes & Fischer, 1977; Greneche & Varret, 1982). In all other cases the scattering matrix reduces to a unit matrix multiplied by a constant and the commutativity is satisfied.

Now let us discuss an example of a two-layered system with specific orientations of the magnetic fields. Inhomogeneities in the sample may occur because of: (i) different directions of hyperfine magnetic fields in different layers, (ii) different magnitudes of these fields, and (iii) both effects (i) and (ii). Although case (iii) is the most general one, in the following we shall treat case (i) for simplicity.

Rotation of the system is shown in Fig. 2. Both layers denoted A and B are of the same thickness and density of resonant nuclei. They differ only in the directions of their hyperfine magnetic fields, given by the unit vectors $\mathbf{m}_A$ and $\mathbf{m}_B$. The scattering lengths N_A and N_B before rotation [Fig. 2(a)] are given as (Hannon & Trammell, 1999; Röhlsberger, 2004)

$$N_A = \frac{3}{16\pi}\begin{pmatrix} F_{+1}+F_{-1} & -i(F_{+1}-F_{-1}) \\ i(F_{+1}-F_{-1}) & F_{+1}+F_{-1} \end{pmatrix}, \quad (5)$$

$$N_B = \frac{3}{16\pi}\begin{pmatrix} 2F_0 & 0 \\ 0 & F_{+1}+F_{-1} \end{pmatrix}. \quad (6)$$

The energy-dependent functions F_M, where $M = -1, 0, 1$, are given by the formula

$$F_M = \frac{-2\pi f_{\rm LM}\Gamma}{k(1+\alpha)(2I_{\rm g}+1)} \sum_{m_{\rm g}} \frac{C^2(I_{\rm g}1I_{\rm e}; m_{\rm g}M)}{E - \Delta E_{m_{\rm g},M} + i\,\Gamma/2}, \quad (7)$$

where $f_{\rm LM}$ is the Lamb–Mössbauer factor, Γ is the natural line width and α is the internal conversion coefficient. $I_{\rm g,e}$ and $m_{\rm g}$ are the spin and magnetic quantum numbers, respectively, of nuclei in the ground and excited states. The energy dependence is given as a sum of Lorentzian lines corresponding to six allowed transitions between the ground and excited states with transition energies $\Delta E_{m_{\rm g},M}$. The amplitudes of the Lorentzian lines depend on the corresponding Clebsch–Gordan coefficients $C(I_{\rm g}1I_{\rm e}; m_{\rm g}M)$.

One can find that the matrices N_A and N_B do not commute. The noncommutativity is essentially ensured by the off-diagonal elements of N_A. In general, off-diagonal elements describe the polarization mixing effect (Blume & Kistner, 1968) and so the measured difference is always accompanied by a change in the radiation polarization during scattering (assuming polarized incident radiation).

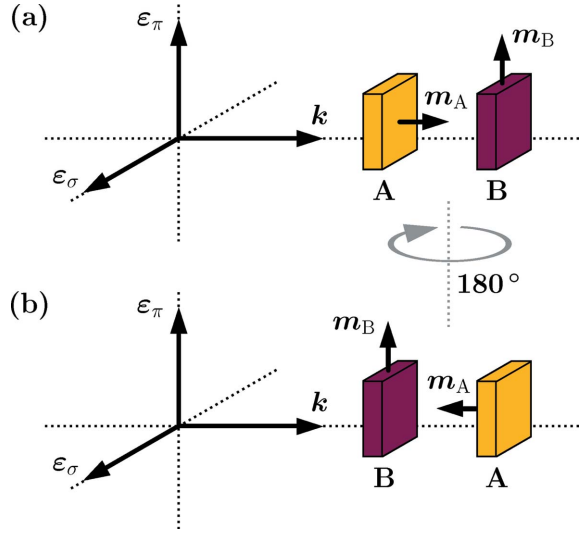

Figure 2
An example of a two-layered scattering system with layers A and B differing in the directions of their hyperfine magnetic fields, which are given by the unit vectors $\mathbf{m}_A$ and $\mathbf{m}_B$. The arrangement shown in panel (b) is obtained from the arrangement in panel (a) by a 180° rotation of the layers around the $\boldsymbol{\varepsilon}_\pi$ axis.

The corresponding scattering matrices are

$$T_A = \exp\left[i(F_{+1}+F_{-1})Kd\right]\begin{pmatrix} C & S \\ -S & C \end{pmatrix}, \quad (8)$$

$$T_B = \begin{pmatrix} \exp(i\,2F_0Kd) & 0 \\ 0 & \exp\left[i(F_{+1}+F_{-1})Kd\right] \end{pmatrix}, \quad (9)$$

where $C = \cos[(F_{+1} - F_{-1})Kd]$, $S = \sin[(F_{+1} - F_{-1})Kd]$ and $K = 3\rho/8k$.

The total scattering matrix after 180° rotation $T^{\rm rot}$ can be expressed as

$$T^{\rm rot} = (T_BT_A)^{\rm rot} = T_A^{\rm rot}T_B^{\rm rot}. \quad (10)$$

The scattering matrices after rotation, $T_A^{\rm rot}$ and $T_B^{\rm rot}$, are equal to the transpose of T_A and T_B, respectively. Therefore, the total scattering matrix $T^{\rm rot}$ is different from T and these two matrices are also related by a transpose.

Simulated spectra corresponding to the discussed two-layered system are presented in Fig. 3. The spectra were calculated for fully $\boldsymbol{\varepsilon}_\sigma$-polarized radiation and unpolarized detection. The intensities of the scattered radiation corresponding to the system before and after rotation around the $\boldsymbol{\varepsilon}_\pi$ axis are presented in the energy and time domains. Differences between the two geometries are demonstrated for varying total thicknesses ranging from 0.1 to 10 μm. In addition, a homogeneous mixture of both layers is also shown for

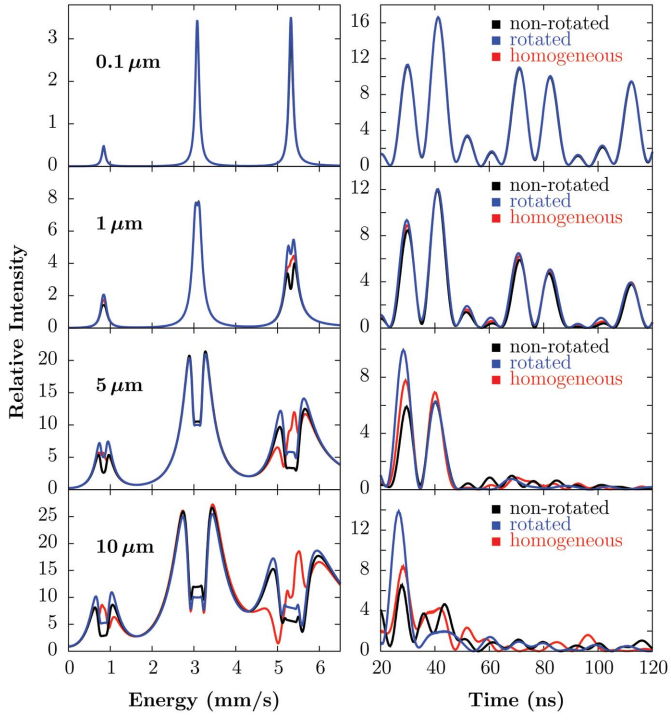

Figure 3
A comparison of simulated energy and time spectra corresponding to three different arrangements of the considered scattering system. The spectra differences increase with increasing total thickness. This is due to the increasing contribution of multiple scattering, where the spatial distribution of the nuclear sites (which is different for the three arrangements) starts to have a more significant impact on the scattering.

comparison. The material parameters of the two layers were selected to match those of α-Fe (with all iron nuclei in the form of ^{57}Fe) at room temperature (Bergmann *et al.*, 1994; Preston *et al.*, 1962). The figures clearly demonstrate the development of the studied phenomenon with increasing thickness. For a relatively thin system, all three cases (non-rotated, rotated and a homogeneous mixture of *A* and *B*) exhibit almost the same features. As the thickness increases, the differences among the signals become more significant.

The thickness dependence reflects the role of multiple scattering in the 180° rotational invariance violation. The non-zero intensity difference comes from photons scattered in both system layers. It is noteworthy that the resonant absorption and re-emission of photons in only one layer are independent of the spatial distribution of nuclear sites along the **k** direction and do not reflect its inhomogeneity. If the material thickness is too small, the multiple scattering is suppressed and 'invariant' photon paths prevail. Consequently, the scattering system behaves as homogeneous and no differences among the time spectra are observed.

2.2. Experimental realization

This part of the paper presents experimental observation of the discussed phenomena. Differences in the time spectra are demonstrated using an $Fe_{81}Mo_8Cu_1B_{10}$ metallic glass. The studied sample was prepared in the form of ribbons with a thickness of approximately 20 µm which were enriched by ^{57}Fe resonant nuclei to around 50%.

For modelling spatially confined magnetic inhomogeneities, one side of the ribbons was irradiated by N^+ ions with an energy of 130 keV and a fluency of 2.5×10^{17} ions cm^{-2}. The implantation conditions caused the formation of a sufficient number of crystallites which subsequently modified the bulk magnetic properties of the studied sample (Miglierini & Hasiak, 2016).

NFS experiments were performed on the ID18 beamline at the ESRF, Grenoble (Rüffer & Chumakov, 1996). The energy of the synchrotron radiation was set to 14.4 keV with a bandwidth of 1 meV, allowing excitation of the ^{57}Fe energy levels.

The sample was measured at room temperature and during isothermal annealing at 573 K when crystallization proceeds. The destination temperature was achieved within 3 min. The sample was held in a vacuum furnace under isothermal conditions for 1 h.

The orientation of the sample was set by fixing it on a stable vertical holder. Two sets of NFS time spectra were accumulated. For each of them a different side of the ribbon was facing the detector. These two cases can be denoted as 'non-rotated' and 'rotated' as they differ only by the 180° rotation of the sample with respect to the $\boldsymbol{\varepsilon}_\pi$ axis.

Fig. 4 shows a pair of time spectra, one for each ribbon orientation, measured at room temperature. Data acquisition took 5 min for both ribbon orientations. The time spectra were normalized to a unit area for mutual comparison.

In the time spectra of the $Fe_{81}Mo_8Cu_1B_{10}$ sample two main contributions can basically be distinguished: low-frequency and high-frequency quantum beats. The low-frequency contribution originates from the amorphous matrix, which is in a paramagnetic state and exhibits quadrupole interactions characterized by a doublet in the energy domain. The high-frequency quantum beats can be assigned to those nuclear sites which exhibit magnetic hyperfine interactions.

The magnetic contributions to the time spectra can be relatively complex, similar to the situation which is encountered in the energy domain (Miglierini & Greneche, 1997*a*). One of them is given by the nanocrystalline grains that are formed in the amorphous matrix and contribute significantly to the sample properties when crystallization takes place. At room temperature, the grains exhibit magnetic splitting of ~31 T. Such a strong hyperfine magnetic field suggests the occurrence of ferromagnetic exchange interactions among the nanocrystalline grains which eventually polarize the amorphous residual matrix (Miglierini & Greneche, 1997*b*). This gives rise to magnetically active amorphous regions which represent another magnetic contribution to the time spectra.

Although the time spectra measured at room temperature are qualitatively very similar [Fig. 4(*a*)], differences can clearly be seen, mainly in the range between 20 and 50 ns [Fig. 4(*b*)]. These differences are in the form of different ratios between the magnetic quantum beats. Therefore, they can be ascribed to an inhomogeneous spatial distribution of the nuclear sites exhibiting magnetic hyperfine interactions.

The magnetic inhomogeneities could be observed even at room temperature, *i.e.* before the ribbons were exposed to the elevated temperature to initiate crystallization. The ribbons already contained a small number of tiny magnetic grains with a relatively high hyperfine magnetic field. These grains were formed during the preparation process and their further development was enhanced by the ion irradiation. Consequently, the presence of the nanocrystals and magnetic amorphous regions is responsible for the clearly recognizable magnetic splitting of the nuclear energy levels which has, in turn, resulted in the high-frequency quantum beats observed in Fig. 4.

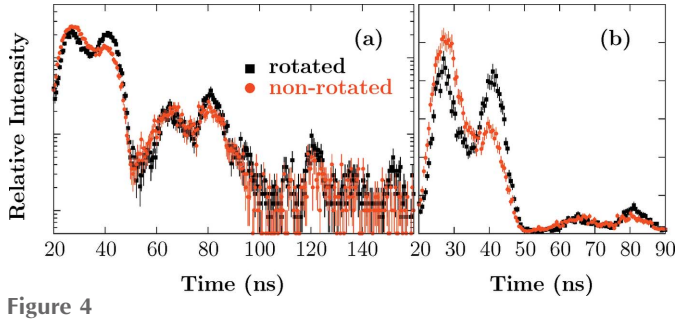

Figure 4
NFS time spectra for the $Fe_{81}Mo_8Cu_1B_{10}$ alloy measured at room temperature before isothermal annealing. (*a*) Full time spectra on a conventional logarithmic scale. (*b*) A detailed plot in the time range with the most significant differences in the time spectra, plotted on a linear scale. The differences in the rotated and non-rotated time spectra arise from the inhomogeneous spatial distribution of the magnetic nuclear sites in the sample.

Fig. 5 shows the evolution of selected time spectra measured during isothermal annealing. Spectra recorded during 3 min of annealing are displayed after different annealing times.

The time spectra acquired during the first 3 min of annealing correspond to the situation where the sample has reached 573 K [Figs. 5(*a*) and 5(*b*)]. With the increase in temperature the originally well resolved magnetic contribution is suppressed. At the same time, the differences in the time spectra have vanished. It can be presumed that this was caused by the suppression of magnetic interactions in the amorphous regions.

Several minutes after the onset of heating, crystallization starts. As the number of magnetic nanocrystalline grains in the sample increases the magnetic quantum beats and also differences in the time spectra reappear [Figs. 5(*c*) and 5(*d*)]. Deviations in the time spectra and differences in their ratios of magnetic quantum beats evolve further with time until about 30 min of annealing [Figs. 5(*e*) and 5(*f*)]. After that they do not change significantly.

The evolution of the differences in the magnetic quantum beats ratios can be ascribed to an increase in the amount of magnetic crystalline phase at the expense of the paramagnetic amorphous matrix. This is analogous to the effect of increasing thickness described previously for the model case of the two-layered scattering system (see Fig. 3 for comparison). This suggests that the violation of the 180° rotational invariance at the elevated temperature originates from inhomogeneity in the hyperfine magnetic field of the crystals. This interpretation is supported by the observed correlation between the evolution of differences in the time spectra and the vanishing and reappearing of high-frequency magnetic quantum beats.

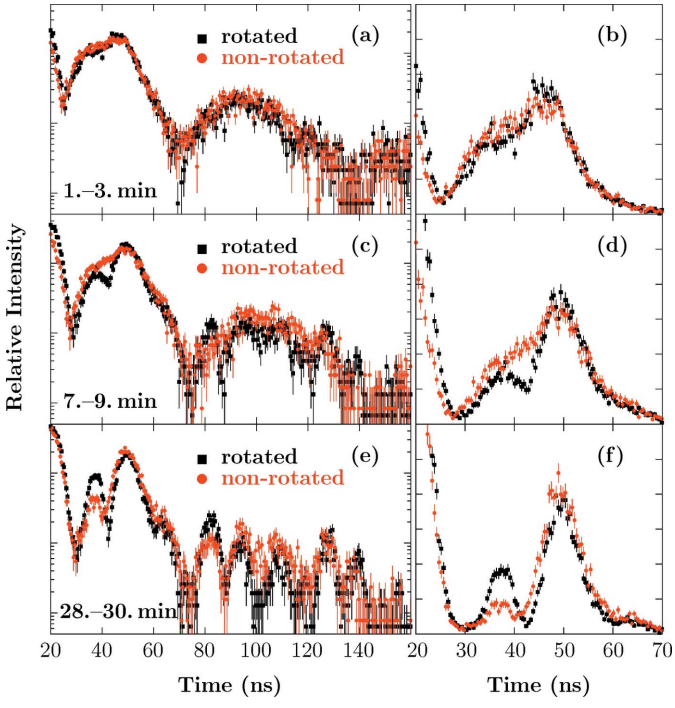

Figure 5
$Fe_{81}Mo_8Cu_1B_{10}$ time spectra during isothermal annealing as full-range logarithmic (left column) and detailed linear (right column) plots. The linear plots clearly show how the differences in the time spectra increase with increasing annealing time. This can be explained by the increasing the number of magnetic nanocrystalline grains exhibiting spatial inhomogeneities.

These NFS experiments allowed the identification of magnetic inhomogeneities in the bulk of the studied sample. The inhomogeneities were observed at room temperature before any thermal treatment and also during isothermal annealing of the ribbons. In the latter, NFS revealed their suppression and subsequent restoration due to the formation of newly emerging nanocrystalline grains in the amorphous matrix. This type of information is not accessible by commonly used experimental techniques. For example, CEMS (conversion electron Mössbauer spectrometry) could be used to examine the effect of ion irradiation in the studied sample, but being a surface-sensitive technique it enables scanning only to a depth of about 200 nm.

This information on magnetic inhomogeneities could be obtained solely by considering the observed rotational invariance violation and its evolution during annealing. For more information a detailed quantitative evaluation of the experimental data would be required. To point out the difficulties with fitting the time spectra, a correct fitting model should include information on the structure (number and thickness of layers) and type (varying magnitudes, directions or both) of the magnetic inhomogeneities. It would also have to reflect the crystallization process, where the parameters could evolve over time. Finally, the fit also requires a proper representation of the magnetic texture in NFS experiments. To the authors' knowledge there is no available software package allowing such a general implementation of the inhomogeneities and the texture. This implementation is beyond the scope of the present work and will be the subject of further research.

3. Conclusions

In conclusion, NFS of synchrotron radiation can be used for the investigation of inhomogeneities of hyperfine interactions. Theoretical analysis based on a model of a multilayered system shows that an inhomogeneous spatial distribution of the nuclear sites can be revealed by NFS experiments performed twice, viz. before and after sample rotation by 180° around one of the polarization axes. In the presence of electric and/or magnetic texture, the inhomogeneities can cause violation of the rotational invariance.

The role of polarization mixing and multiple scattering in the time spectra differences and their dependence on the thickness are demonstrated by a two-layered system exhibiting different magnetic orientations.

The approach of conducting NFS experiments for two sample orientations differing by a 180° rotation was successfully applied in the study of an $Fe_{81}Mo_8Cu_1B_{10}$ metallic glass and its crystallization during isothermal annealing. Analysis of the pairs of the measured time spectra revealed the presence of spatially inhomogeneous magnetic regions. They are affected by newly formed nanocrystals that are predominantly located on that side of the ribbons which was exposed to the ion irradiation.

Acknowledgements

The nuclear forward-scattering experiments were performed on beamline ID18 at the European Synchrotron Radiation Facility (ESRF), Grenoble, France. We are grateful to R. Rüffer at the ESRF for providing assistance in using beamline ID18. We would also like to thank Helena Sedláčková (Palacký University Olomouc, Czech Republic) for her help with preparation of the manuscript.

Funding information

Funding for this research was provided by: internal IGA grant of Palacký University (IGA_PrF_2018_002); Project VEGA 1/0182/16.

References

Atzmony, U., Norton, S. J., Swartzendruber, L. J. & Bennett, L. H. (1987). *Nature*, **330**, 153–154.
Bergmann, U., Shastri, S. D., Siddons, D. P., Batterman, B. W. & Hastings, J. B. (1994). *Phys. Rev. B*, **50**, 5957–5961.
Blume, M. & Kistner, O. C. (1968). *Phys. Rev.* **171**, 417–425.
Cashion, J. D., Weiser, P. S., McGrath, A. C., Pollard, R. J. & Smith, T. F. (1990). *Hyperfine Interact.* **58**, 2507–2512.
Deák, L., Bottyán, L., Fülöp, T., Kertész, G., Nagy, D. L., Rüffer, R., Spiering, H., Tanczikó, F. & Vankó, G. (2012). *Phys. Rev. Lett.* **109**, 237402.
Greneche, J. M. & Varret, F. (1982). *J. Phys. C Solid State Phys.* **15**, 5333–5344.
Hannon, J. P. & Trammell, G. T. (1999). *Hyperfine Interact.* **123/124**, 127–274.
L'Abbé, C., Callens, R. & Odeurs, J. (2001). *Hyperfine Interact.* **135**, 275–294.
Machala, L., Procházka, V., Miglierini, M., Sharma, V. K., Marušák, Z., Wille, H. C. & Zbořil, R. (2015). *Phys. Chem. Chem. Phys.* **17**, 21787–21790.
Miglierini, M. & Greneche, J. M. (1997*a*). *J. Phys. Condens. Matter*, **9**, 2303–2319.
Miglierini, M. & Greneche, J. M. (1997*b*). *J. Phys. Condens. Matter*, **9**, 2321–2347.
Miglierini, M. & Hasiak, M. (2016). *Phys. Status Solidi A*, **213**, 1138–1144.
Miglierini, M., Pavlovič, M., Procházka, V., Hatala, T., Schumacher, G. & Rüffer, R. (2015). *Phys. Chem. Chem. Phys.* **17**, 28239–28249.
Miglierini, M., Procházka, V., Stankov, S., Svec, P., Zajac, M., Kohout, J., Lancok, A., Janickovic, D. & Svec, P. (2012). *Phys. Rev. B*, **86**, 020202.
Pfannes, H.-D. & Fischer, H. (1977). *Appl. Phys.* **13**, 317–325.
Preston, R. S., Hanna, S. S. & Heberle, J. (1962). *Phys. Rev.* **128**, 2207–2218.
Röhlsberger, R. (2004). *Nuclear Condensed Matter Physics With Synchrotron Radiation: Basic Principles, Methodology and Applications.* Berlin: Springer-Verlag.
Rüffer, R. (2002). *Hyperfine Interact.* **141/142**, 83–97.
Rüffer, R. & Chumakov, A. I. (1996). *Hyperfine Interact.* **97–98**, 589–604.
Smith, P. R., Cashion, J. D. & Brown, L. J. (1992). *Hyperfine Interact.* **71**, 1503–1506.
Sturhahn, W. & Gerdau, E. (1994). *Phys. Rev. B*, **49**, 9285–9294.
Vogl, G. & Sepiol, B. (1999). *Hyperfine Interact.* **123/124**, 595–609.